SCIENTIFIC REP⚙RTS

OPEN

Gap state analysis in electric-field-induced band gap for bilayer graphene

Kaoru Kanayama[1] & Kosuke Nagashio[1,2]

The origin of the low current on/off ratio at room temperature in dual-gated bilayer graphene field-effect transistors is considered to be the variable range hopping in gap states. However, the quantitative estimation of gap states has not been conducted. Here, we report the systematic estimation of the energy gap by both quantum capacitance and transport measurements and the density of states for gap states by the conductance method. An energy gap of ~250 meV is obtained at the maximum displacement field of ~3.1 V/nm, where the current on/off ratio of ~3×10^3 is demonstrated at 20 K. The density of states for the gap states are in the range from the latter half of 10^{12} to 10^{13} eV^{-1}cm^{-2}. Although the large amount of gap states at the interface of high-k oxide/bilayer graphene limits the current on/off ratio at present, our results suggest that the reduction of gap states below ~10^{11} eV^{-1}cm^{-2} by continual improvement of the gate stack makes bilayer graphene a promising candidate for future nanoelectronic device applications.

The main issue of downscaling in the Si field-effect transistors (FETs) is the short channel effect in which the gate control is weakened by the drain bias. Based on an analysis of the electrical potential distribution in the channel region, it is well known that the short channel effect can be neglected when the channel length is ~6 times longer than the scaling length $\lambda = \sqrt{(\varepsilon_{ch} t_{ch} t_{ox})/(N \varepsilon_{ox})}$ [1,2], where N, ε_{ch}, ε_{ox}, t_{ch}, and t_{ox} are the effective gate number, dielectric constants for the channel and gate insulator, and thickness of the channel and the gate oxide. This perspective attracts great attention to two-dimensional (2D) layered channels in the FET application because of their rigidly controllable atomic thickness ($t_{ch} < 1$ nm), as well as the low dielectric constant ($\varepsilon_{ch} = \sim 4$) for typical 2D layered channels[3,4]. Although old-but-new 2D channels, such as transition metal dichalcogenides, black phosphorus, and so on, have been intensively investigated recently[5–9], bilayer graphene with an electrostatically tunable band gap still has an advantage over the high performance device from the viewpoint of mobility due to the smaller effective mass ($m_{BLG} = \sim 0.037$[10], $m_{BP} = 0.13$[11], and $m_{MoS2} = \sim 0.37$[12]).

The suppression of conductivity in bilayer graphene has so far been reported by many researchers by applying an external electrical field[13–24]. Optical spectroscopic measurements, such as angle-resolved photoemission spectroscopy[25] and infrared spectroscopy[14,26,27], confirmed the band gap formation. However, the large current on/off ratio (I_{on}/I_{off}) of ~10^6 is obtained only at the quite low temperature of 300 mK[17], not at room temperature. The reason is explained by the variable range hopping in gap states[13,15,17–19]. Therefore, the main target issue for bilayer graphene is a low current on/off ratio at room temperature. At the zero-order approximation, there will intrinsically be no interface states in bilayer graphene because there are no dangling bonds on the basal plane, compared with P$_b$ centers in the SiO$_2$/Si system, assigned by the electron spin resonance measurement[28–30]. Although the strong disorder at the channel edge was expected to act as a main conduction path, the transport measurement in the Corbino geometry excluded this idea[19]. The origin of the gap states remains an open question. So far, detailed measurements on the density of states (D_{it}) and the time constant (τ_{it}) for gap states have not been reported.

[1]Department of Materials Engineering, The University of Tokyo, Tokyo 113-8656, Japan. [2]PRESTO, Japan Science and Technology Agency (JST), Tokyo 113-8656, Japan. Correspondence and requests for materials should be addressed to K.N. (email: nagashio@material.t.u-tokyo.ac.jp)

Contrary to the transport measurement, the extraction of the quantum capacitance (C_Q) through the capacitance measurements (*C-V*) of bilayer graphene provides direct information on the density of states (*DOS*) of bilayer graphene, consequently, the energy gap (E_G), because it is regarded as the energy cost of inducing the carriers in graphene and is directly related as $C_Q = e^2 DOS$[31]. Although there are a few reports on C_Q measurement for bilayer graphene[32–34], the comparison of E_G estimated both from *I-V* and *C-V* has not been done yet. Moreover, in principle, the mobile carrier response to a small-signal alternating current voltage at a certain frequency is measured in the *C-V* measurement. The capture and emission process of mobile carriers at the trap levels distributed throughout the band gap can be extracted as a deviation from the ideal carrier response without any trap levels under the assumption of the equivalent circuit. This technique is known as the conductance method[34].

In this work, we present the systematic extraction of E_G as a function of the displacement field ($\overline{D}$), which determines the band structure of bilayer graphene, from both *I-V* and *C-V*. The conductance measurements are carried out to extract D_{it} and τ_{it}; then, the possible origins of the gap states are discussed.

Bilayer graphene FTEs with a high quality top gate insulator

Recently, we have demonstrated a considerable suppression of the low-field leakage through high-*k* Y_2O_3 on monolayer graphene by applying high-pressure O_2 annealing[35]. The same process was applied to bilayer graphene FETs. The improved electrical quality of the insulators provides access to the large displacement field ($\overline{D} = \sim 3.1 \, V/nm$) in this study. Although there are several conventions for $\overline{D}$, we adopt the most widely used definition of $\overline{D} = 1/2 [\varepsilon_{BG}/d_{BG}(V_{BG} - V_{BG}^0) - \varepsilon_{TG}/d_{TG}(V_{TG} - V_{TG}^0)]$ in this study[14], where ε_{BG}, ε_{TG}, d_{BG}, d_{TG}, V_{BG}, and V_{TG} are the dielectric constants, the insulator thickness, and the gate voltages for back- and top-gate insulators, respectively. (V_{TG}^0, V_{BG}^0) is the charge neutrality point to give the minimum resistance in the top-gated region.

To suppress the hysteresis in drain current—gate voltage curves, the SiO_2 surface was converted to be hydrophobic (siloxane group) by annealing the SiO_2/Si substrate in a 100% O_2 atmosphere at 1000 °C prior to the graphene transfer[36]. Then, the conventional back-gated bilayer graphene FETs containing source and drain electrodes were fabricated on $\sim 90 \, nm$ SiO_2/n$^+$-Si substrates by the mechanical exfoliation of Kish graphite. This device was annealed under Ar/H$_2$ gas flow at 300 °C for 3 hours to remove the resist residue on the bilayer graphene channel. Subsequently, Y_2O_3, with a thickness of $\sim 6 \, nm$, was deposited on bilayer graphene FETs by the thermal evaporation of Y metal in the O_2 atmosphere at $P_{O2} = 10^{-1} \, Pa$[35]. Then, high-pressure annealing was carried out in a 100% O_2 atmosphere at $\sim 100 \, atm$ and 300 °C. Finally, the top gate electrode was patterned, followed by annealing at 300 °C for 30 s under 0.1% O_2 gas flow. The lack of a Raman D band measured through Y_2O_3 indicated that no detectable defects were introduced into the bilayer graphene by the high-pressure O_2 annealing, as shown in Supplementary Fig. S1c.

Estimation of E_G by *C-V* and *I-V*

We first focus on the capacitance measurement to determine E_G through the C_Q extraction. Figure 1a shows the total capacitance (C_{Total}) between the source and top gate electrodes, obtained by sweeping V_{TG} at different V_{BG}, which were measured at the frequency of 1 MHz in a vacuum of $\sim 1 \times 10^{-5} \, Pa$ at 20 K. Figure 1b is the counter plot of C_{Total}. The C_{Total} reduction at the Dirac point with increasing V_{BG} indicates the decrease in the *DOS* by the gap formation because of the strong contribution of C_Q. The hysteresis in the bidirectional *C-V* curves is quite small ($\sim 0.1 \, V$ for a $V_{TG} = \pm 4 \, V$ sweep)[35]. As shown in Supplementary Fig. S2, the frequency dependence of C_{Total} is clearly observed in the gap region, suggesting the existence of trap sites. The gradual saturation of the capacitance with increasing frequency from 200 kHz to 1 MHz suggests that C_{Total} measured at 1 MHz is close to the ideal capacitance without any response to the trap site. Therefore, the *C-V* measurement in Fig. 1a was carried out at 1 MHz.

The slope of the dotted black line at the charge neutrality point of (V_{TG}^0, V_{BG}^0) = 0.75, 9 in Fig. 1b corresponds to the capacitive coupling ratio between the top gate and back gate, that is, $-0.0412 = -C_{BG}/C_{TG}$. Using $C_{BG} = 0.038 \, \mu F cm^{-2}$ for SiO_2 with $d_{BG} = 90 \, nm$ and $\varepsilon_{BG} = 3.9$, C_{TG} is estimated to be $0.93 \, \mu F cm^{-2}$. In the course of this study, the typical C_{TG} value is $\sim 1.2 \, \mu F cm^{-2}$, depending on the Y_2O_3 thickness. The C_{TG} value is considerably high compared with those reported previously for both monolayer and bilayer graphene, as shown in Fig. 1c. Based on C_{TG} and C_{BG}, the white dotted lines indicate the constant $\overline{D}$, whose values are shown at the periphery of the counter plot of Fig. 1b. The maximum $\overline{D}$ at the Dirac point in this study is $\sim 3.1 \, V/nm$, which is quite high compared with other reports.

The simplified equivalent circuit model of the device is shown in Fig. 2a, where V_{ch} and C_{para} are the charging voltage and the parasitic capacitance. The Fermi energy (E_F) and the band structure of bilayer graphene are independently controlled by changing V_{TG} and V_{BG}. It should be noted that the contribution of C_{BG} is implicitly involved in C_{Total} through C_Q and V_{ch}, in Fig. 2a. Based on the equivalent circuit of Fig. 1a, C_Q was extracted along the constant $\overline{D}$ lines, i.e., the constant band structure, by using C_{para} as a fitting parameter. Figure 2b shows C_Q as a function of E_F for different constant $\overline{D}$ values. At $\overline{D} = 0 \, V/nm$, the extracted C_Q is fitted reasonably well with the theoretical value for bilayer graphene calculated by the tight-binding model[37] by selecting $C_{para} = 0.91 \, \mu F cm^{-2}$. The charging energy required to induce carriers in bilayer graphene is denoted by E_F, which is expressed as $E_F = eV_{ch}$. V_{ch} can be expressed by the
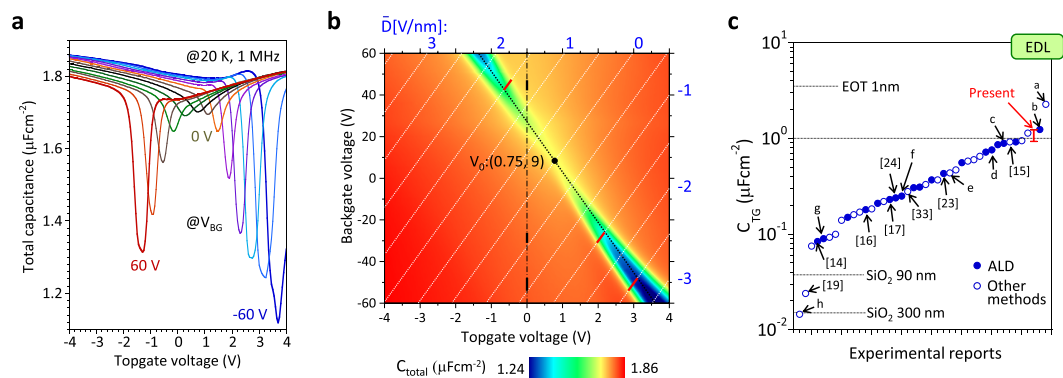
Figure 1. Capacitance characteristics of dual gated bilayer graphene FETs. (**a**) C_{Total} between the source and top gate electrodes as a function of V_{TG} for different V_{BG} measured at 20 K and a frequency of 1 MHz. (**b**) Counter plot of C_{Total}. The charge neutrality point is (V_{TG}^0, V_{BG}^0) = 0.75, 9. The $\overline{D}$ value is shown at the periphery of the counter plot. (**c**) Comparison of C_{TG} with those reported previously for both monolayer and bilayer graphene. Closed and open circles indicate C_{TG} obtained for oxide insulators deposited by the atomic layer deposition technique (ALD) and for insulators prepared by another technique, respectively. "EOT" and "EDL" indicate C_{TG} obtained for 1 nm-thick-SiO_2 and a typical electric double-layer, respectively. Several papers are included. a: Zhang, Z. *et al. Appl. Phys. Lett.* **101,** 213103 (2012). b: Fallahazad, B. *et al. Appl. Phys. Lett.* **100,** 093112 (2012). c: Zou, K. *et al. Nano Lett.* **13,** 369 (2013). d: Meric, I. *et al. Nature Nanotech.* **3,** 654 (2008). e: Liao, L. *et al., Nature* **467,** 305 (2010). f: Kim, S. *et al. Appl. Phys. Lett.* **94**, 062107 (2009). g: Wu, Y. *et al. Nature* **472,** 74 (2011). h: Velasco Jr. J. *et al. Nature Nanotech.* **7,** 156 (2012).
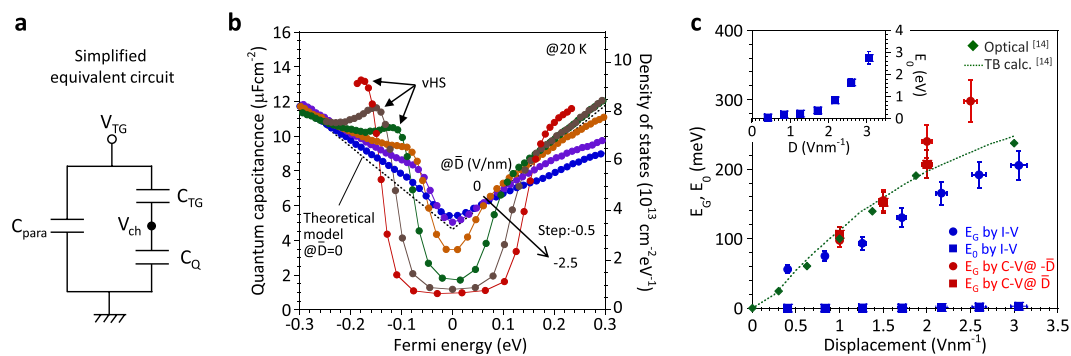

Figure 2. Quantum capacitance and energy band gap. (**a**) Simplified equivalent circuit for the bilayer graphene FET. (**b**) C_Q as a function of E_F at different $\overline{D}$ ranging from ~0 to −2.5 V/nm. The right vertical axis indicates *DOS*. (**c**) E_G and E_0 as a function of absolute value for $\overline{D}$ determined from the *C-V* data and *I-V* data.

equation for a series combination of capacitors according to $V_{ch} = V_{TG}' - \int_0^{V_{TG}'} C_{Total}' / C_{Y2O3} dV_{TG}'$, where C_{Total}' and V_{TG}' are defined as $C_{Total}' = C_{Total} - C_{para}$ and $V_{TG}' = V_{TG} - V_{DP}$, respectively. V_{DP} is the Dirac point voltage. The detailed calculation method is explained in Supplementary Fig. S3. The C_Q value at the Dirac point for $\overline{D}$ = 0 V/nm is consistent well with the theoretical value because the *DOS* for bilayer graphene at the Dirac point is larger than the residual carriers induced externally by the charged impurities at the SiO_2 surface[38]. With increasing $\overline{D}$, the reduction of C_Q is clearly observed because the scattering issue, which strongly contributes to the conductivity in *I-V*, can be neglected in *C-V*. It should be emphasized that the *DOS* within the gap region almost reaches zero, which is not observed in the previous report for bilayer graphene with the h-BN top gate[33]. Moreover, the van Hove Singularity (vHS) is also observed near the valence band edge, as shown by arrows. The appearance of the vHS is asymmetric, that is, a valence band edge for negative $\overline{D}$ and a conduction band edge for positive $\overline{D}$ (not shown in Fig. 2b), which is consistent with previous data[33]. This phenomenon is explained by the near-layer capacitance enhancement effect[39]. Figure 2c shows E_G as a function of absolute value for $\overline{D}$, determined from the *C-V* data. E_G was defined as the energy between inflection points for the conduction and valence sides in Fig. 2b. E_G is roughly ~300 mV at $\overline{D}$ = 2.5 V/nm.
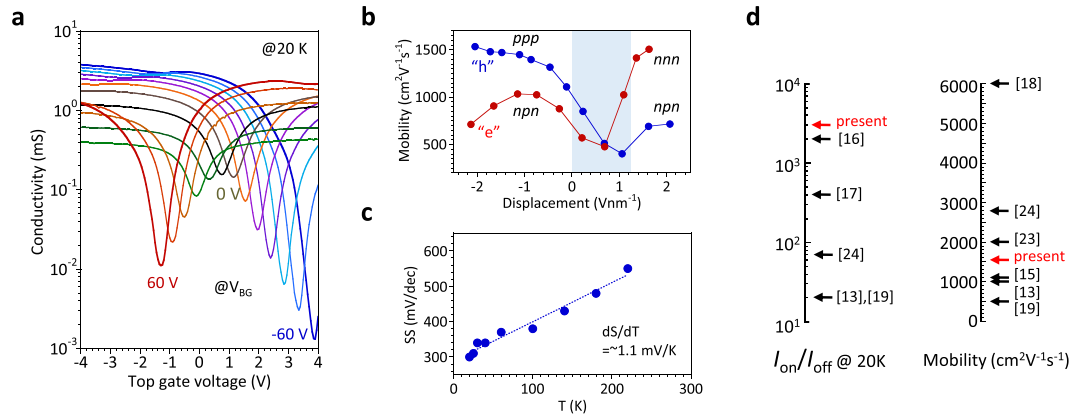
Figure 3. Transport characteristics. (a) σ as a function of V_{TG} for different V_{BG} measured at 20 K. The drain current is on the order of 50 mA for the drain voltage of 100 mV. The leakage current is ~10^7 orders of magnitude lower than the drain current, as shown in Supplementary Fig. S1d. (b) Maximum mobility as a function of $\overline{D}$ for different regions of *pnp*, *ppp*, *npn*, and *nnn*. The mobility at the hatched region ($0 < \overline{D} < 1.2$) is relatively low because of the contribution of the ungated region between the top gate and source/drain electrodes (Supplementary Fig. S4). (c) Subthreshold swing (*S*) as a function of temperature. The slope is nearly linear (dS/dT = ~1.1 mV/K). (d) Comparison of I_{on}/I_{off} and mobility with those reported previously for bilayer graphene. The temperature for I_{on}/I_{off} data was fixed at 20 K. For the mobility, the temperature is not limited to 20 K, and both two-probe and four-probe data are shown here.

We now consider the transport properties for the same device. Figure 3a shows the conductivity (σ) measured as a function of V_{TG} for different V_{BG} at 20 K. The conductivity at the Dirac point decreases with increasing V_{BG}, again indicating the band gap opening. The maximum I_{on}/I_{off} is ~3×10^3 for $\overline{D} = $~3.1 V/nm. Figure 3b shows the maximum mobility as a function of $\overline{D}$ for different regions of *pnp*, *ppp*, and so on, whose positions are shown in Supplementary Fig. S4a. In terms of the determination of carrier mobility using the Drude model ($\sigma = en\mu$), the carrier density (n) is estimated by the integration of the differential capacitance of C'_{Total}, that is, $n = 1/e \int_0^{V'_{TG}} C'_{Total} dV'_{TG}$, because of the large contribution of C_Q. Otherwise, n is overestimated. However, the carrier density at the access region between the source (drain) and topgate is assumed to be consistent with that at the main channel region just below the topgate electrode for the mobility estimation. Shortening this access region by the self-alignment process[40] is important to extract the mobility more precisely and to improve the device performance.

Moreover, the subthreshold swing (*S*) is plotted as a function of temperature, as shown in Fig. 3c. The *S* value (~600 mV/dec) extrapolated to room temperature is considerably larger than the theoretical lower limit of 60 meV/dec at room temperature[41], suggesting the large contribution of the gap states. Figure 3d compares the present mobility and I_{on}/I_{off} at 20 K with previously reported data. All the data for I_{on}/I_{off} are selected at 20 K from the literature, while the temperature for the mobility is not limited to 20 K. The mobility in the present study is not very high because it includes the contact resistance. In contrast, I_{on}/I_{off} in the present study is quite high in spite of the direct deposition of high-*k* oxide on bilayer graphene without any organic buffer layer.

To determine E_G from the viewpoint of the transport, we study the temperature dependence of σ at different $\overline{D}$ ranging from 0 to 3.1 V/nm. Figure 4a shows the temperature dependence of σ as a function of $V_{TG} - V_{DP}$ at $V_{BG} = -60$ V. So far, the temperature dependence of the conductivity in bilayer graphene is explained by the sum of three terms, the thermal activation (TA) at the high temperature region, nearest neighbor hopping (NNH) at the intermediate temperature range and variable range hopping (VRH) in a two-dimensional system of localized states at the low temperature region, as follows[17,18],

$$\sigma_{Total} = \sigma_{TA}^0 \exp\left[-\frac{E_G}{2k_BT}\right] + \sigma_{NNH}^0 \exp\left[-\frac{E_0}{k_BT}\right] + \sigma_{VRH}^0 \exp\left[-\left(\frac{T_0}{T}\right)^{1/3}\right], \tag{1}$$

where σ_{TA}^0, σ_{NNH}^0 and σ_{VRH}^0 are prefactors and E_0, T_0 and k_B are the activation energy, the hopping energy and the Boltzmann constant. Since the lowest temperature in this study is 20 K, the contribution of VRH may not be observed. The conductivity at the Dirac point is plotted as a function of temperature and fitted by two combinations of TA + NNH and TA + VRH, as shown in Fig. 4b,c, respectively. All the conductivity data are well fitted with respect to T^{-1} for TA + NNH, while the plot with respect to $T^{-1/3}$ does not show clear linear behavior below T = 100 K. The present data can be explained by TA + NNH for the temperature range above 20 K. This is consistent with the previous report where VRH was
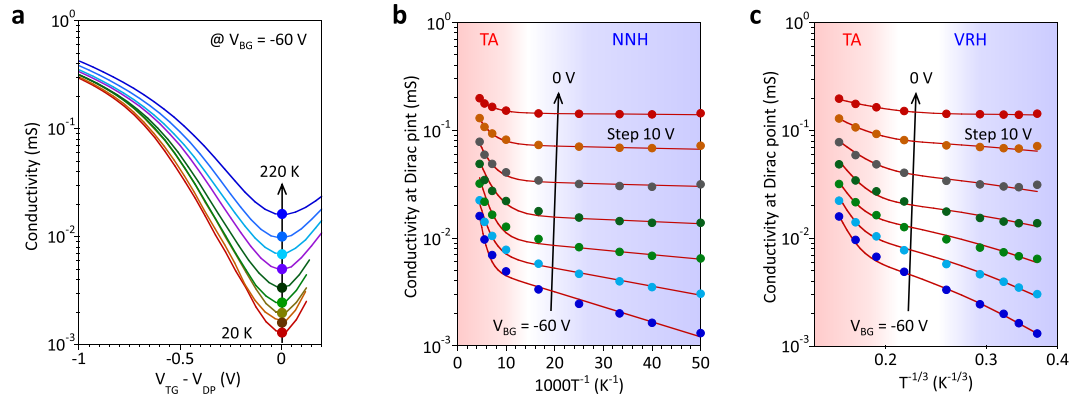
Figure 4. Temperature dependence of conductivity at the Dirac point. (a) Temperature dependence of σ as a function of $V_{TG} - V_{DP}$ at $V_{BG} = -60$ V. **(b,c)** σ at the Dirac point as a function of temperature for different V_{BG} ranging from -60 to 0 V. All the data are fitted by a sum of TA and NNH for (**b**) and by a sum of TA and VRH for (**c**).

observed at below 5 K[13,17,18]. Extracted E_G and E_0 are plotted as a function of $\overline{D}$ in Fig. 2c, respectively, along with the results obtained in infrared absorption studies[14]. E_G determined by *I-V* is reasonably consistent with the previous infrared absorption data, while E_G determined by *C-V* is slightly larger. This difference is discussed later. Moreover, E_0 increases with $\overline{D}$ and reaches 2.8 meV at $\overline{D} = 3.1$ V/nm, which is high compared with previous reports[18].

Estimation of D_{it} and τ_{it}

To gain insight into the interface properties, the gap states in the electrostatically opened-band gap are quantitatively analyzed using the conductance method. The equivalent circuit of the device is shown in the left of Fig. 5a, where R_{it} and C_{it} are the resistance and capacitance associated with the interface traps, their product $C_{it}R_{it}$ is defined as τ_{it}, and R_s is the series resistance. It should be noted that R_{it} and C_{it} have been neglected due to roughly no electrical communication of carriers with trap sites at 1 MHz in Fig. 2a. Here, when this equivalent circuit is converted into C_p, in parallel with G_p, as shown in the right of Fig. 5a, the relation between G_p and D_{it} can be given as the following[42],

$$\frac{G_p}{\omega} = \frac{eD_{it}}{2\omega\tau_{it}} ln\left(1 + (\omega\tau_{it})^2\right), \tag{2}$$

where $\omega = 2\pi f$ (*f*: measured frequency). Finally, D_{it} and τ_{it} can be obtained as $D_{it} = (G_p/\omega)_{max}/0.402e^2$ and $\tau_{it} = 1.98/2\pi f_0$, where f_0 is the frequency at $(G_p/\omega)_{max}$. The accurate estimation of D_{it} is possible because G_p/ω does not include C_Q, which is the advantage of the conductance method. However, if there is leakage conductance (G_{leak}), indicated by the dotted line in the left of Fig. 5a, it is quite difficult to separate the two conductance contributions. The key issue to extract D_{it} quantitatively is the fabrication of a highly reliable top gate insulator on bilayer graphene without any leakage current. This has been achieved by the high-pressure O_2 post-deposition annealing of Y_2O_3.

Figure 5b shows G_p/ω as a function of *f* for E_F from -74 to -28 meV, where the band structure was fixed as constant at $\overline{D} = -1.5$ V/nm, i.e., $E_G = \sim 150$ meV. It should be emphasized that G_p was measured under the constant band structure along the constant $\overline{D}$ line by controlling V_{TG} and V_{BG} at the same time. To prevent the contribution of a minority carrier response to the conductance, especially for small band gap semiconductors, the measurement temperature was lowered as much as possible, i.e., 20 K ($k_B T = \sim 1.7$ meV). This quite low temperature is only possible in bilayer graphene because the majority carriers do not freeze due to the doping by the external gate control, unlike substitutionally doped semiconductors. The more detailed measurement conditions are described in the method section. Clear peaks were observed in the G_p/ω-*f* relation, suggesting the detection of a trap-detrapping sequence of carriers with gap states. The τ_{it} value is evaluated to be $\sim 4\,\mu$s. In Fig. 2a, it is assumed that the contribution of C_{it} is roughly negligible in C_{Total}, measured at 1 MHz. According to this τ_{it} value, this assumption is roughly, but not completely, reasonable. Therefore, E_G estimated by *C-V* may be slightly overestimated due to the contribution of C_{it}. Figure 5c shows D_{it} as a function of E_G for different $\overline{D}$. D_{it} is in the range from the latter half of 10^{12} to 10^{13} eV^{-1}cm^{-2}. The energy dependence of D_{it} is not so obvious. Although this value is slightly smaller than that for MoS_2[43], it is larger compared with those of Si[44]. The large amount of gap states at the interface of high-*k* oxide/bilayer graphene limits I_{on}/I_{off} at present. The much lower D_{it} could be achieved for dual-gate bilayer graphene heterostructure with *h*-BN.
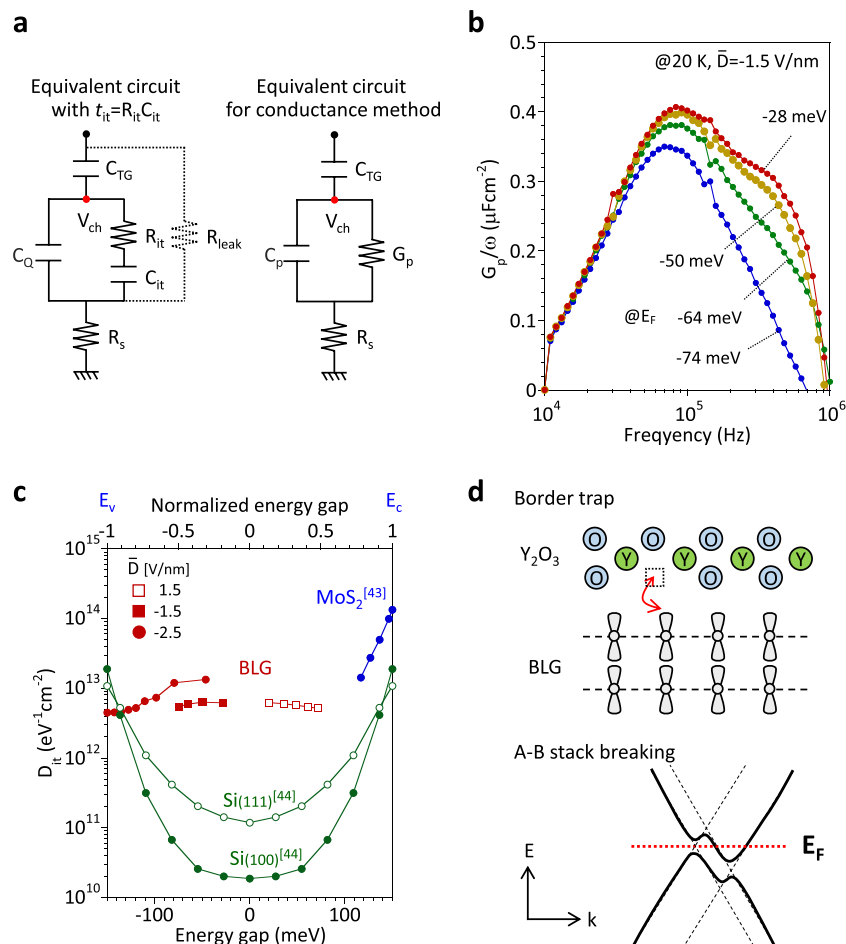
Figure 5. Characterization of gap states. (**a**) The equivalent circuits with $\tau_{it} = R_{it}C_{it}$ (left) and for the conductance method (right). (**b**) G_p/ω as a function of f at $\overline{D} = -1.5\,\text{V/nm}$, i.e., the constant band structure with $E_G = \sim150\,\text{meV}$. E_F was changed from -74 to $-28\,\text{meV}$. (**c**) D_{it} of bilayer graphene (BLG) as a function of E_G for different $\overline{D}$. For comparison, D_{it} for Si(100), Si(111)[44] and MoS$_2$[43] are also included as a function of normalized energy gap (top transverse axis). (**d**) Two possible origins of the gap states are shown. For the border trap (top), some defect sites in oxides, such as an oxygen vacancy (dotted box), work as trap sites. For A-B stack breaking (bottom), the band structure is not ideal but is like the dotted line. When the external electrical field is applied, the band gap is opened, like the solid line.

In general, the conductance method is applied to the metal-oxide-semiconductor (MOS) capacitor, where the current is injected from the back side through the semiconductor substrate, whose series resistance, including back side contact, can be removed by measuring the impedance at the high-frequency limit (see Method). The interface trap conductance can be precisely measured. In contrast, in the present FET structure, the carriers are injected from the side of the channel through the source and drain[43,45]. The channel resistance may contribute to G_p in the equivalent circuit. To avoid this, a device with a relatively short channel was used at the expense of the channel area, which increased C_{para} in this study compared with typical value of $\sim0.2\,\mu\text{Fcm}^{-2}$[35]. Supplementary Figure S5b compares τ_{it} with the channel time constant ($\tau_{ch} = R_{DP}C_{DP}$, where R_{DP} and C_{DP} are the measured resistance and capacitance at the Dirac point), suggesting that τ_{it} is dominant. Therefore, the present D_{it} measurement is reliable.

Finally, let us discuss the origin of the gap states. As mentioned before, no detectable defects are observed by the Raman D band. Therefore, the trap sites formed by defects are ignored in this discussion. Two possible origins are discussed here, as shown in Fig. 5d. One is the external origin, that is, the border trap[46]. The carriers in bilayer graphene electrically communicate with trap sites, such as the oxygen vacancy (dotted box) at the surface of oxides, because π electrons stay on the surface of bilayer graphene. The other is the internal origin. The local breakdown of A-B stacking[47,48] results in the stacking of two monolayers[49], leading to the different band structure. In this case, E_F stays within E_G at some momentum space, while the real states exist at another momentum space, which may macroscopically act as gap states. Here, let us consider the dominant origin of the gap states. From the viewpoint of the time constant, the former origin will be a more time-consuming process than the latter because the rate limiting process is the tunneling between bilayer graphene and trap sites at the oxide surface[50]. On the other hand,

if A-B stack breaking is the dominant origin of the gap states, D_{it} should decrease with increasing $\overline{D}$, which is consistent with the observation in Fig. 2b. This, however, does not appear to be clear in the conductance measurement in Fig. 5c because other devices show almost no difference in D_{it} for different $\overline{D}$. If T_0 in VRH is extracted at the low temperature region below 5 K, the $\overline{D}$ dependence of D_{it} can be discussed more in detail because T_0 is inversely proportional to the density of states for the localized states[51]. Further detailed measurements are required to understand the $\overline{D}$ dependence of D_{it}. Although it is difficult to determine the dominant origin of the gap states at present, the quantitative recognition of the current status for D_{it} in this study does provide the realistic comparison with other semiconductor channels in terms of the interface quality.

Conclusions

We have succeeded in extracting critical information on the interface quality, that is, D_{it} and τ_{it} for gap states. At the large displacement field of ~3 V/nm, they are in the range from the latter half of 10^{12} to 10^{13} eV^{-1}cm^{-2} and ~4 μs, respectively. The large amount of gap states at the interface of high-k oxide/bilayer graphene limits the I_{on}/I_{off} ratio at present. Many trials to characterize the interface properties for other 2D layered channels, as well as bilayer graphene, will help in understanding the origin of the gap states. The improvement of gap states below ~10^{11} eV^{-1}cm^{-2} is the first step for bilayer graphene devices to be a promising candidate for future nanoelectronic applications.

Methods

The transport measurement of the device was performed using a Keysight B1500A semiconductor analyzer in a Nagase low-temperature prober in a vacuum of ~10^{-5} Pa. The capacitance measurement and conductance method under the constant $\overline{D}$ conditions were performed by controlling both the Keysight 4980 A LCR meter and the Keithley 2450 source meter for the back gate. The top gate electrode was connected to the high terminal, while the source and drain electrodes was connected to the low terminal. For the conductance measurement, G_p should be measured accurately by reducing the contribution of R_s in the equivalent circuit in the right side of Fig. 5a. Therefore, ozone treatment was performed for 5 min before the metal deposition to remove the resist residue at the source/drain contact[52], which reduces the contact resistance. Then, R_s was estimated as follows. For the equivalent circuit in Fig. 5a (right), the impedance (Z) is given by $Z = \frac{1}{j\omega C_{TG}} + \frac{1}{j\omega C_p + G_p} + R_s = \left[\frac{G_p}{\omega^2 C_p^2 + G_p^2} + R_s\right] - j\left[\frac{1}{\omega C_{TG}} + \frac{\omega C_p}{\omega^2 C_p^2 + G_p^2}\right] = Z' - jZ''$. Therefore, R_s at the accumulation side was estimated to be 29.4 kΩ by taking the high-frequency limit ($\omega \to \infty$), as shown in Supplementary Fig. S5a. Finally, G_p can be accurately estimated by removing R_s in the equivalent circuit in the right side of Fig. 5a. For the D_{it} measurement at the valence band side, E_F is scanned along negative $\overline{D}$ (−1.5 and −3 V/nm). The access region modulated only by the back gate is always p-type (black line on the dashed-dotted vertical line at $V_{TG} = 0$ V in Fig. 1b), from which a hole is injected into the main channel under the top gate to ensure majority carrier response, and vice versa for the conduction band side at the positive $\overline{D}$. Therefore, D_{it} distributed throughout E_G can be measured using the single FET device, unlike the MOS capacitor.

References

1. Ferain, I., Colinge, C. A. & Colinge, J. -P. Multigate transistors as the future of classical metal-oxide-semiconductor filed-effect transistors. *Nature* **479,** 310–316 (2011).
2. Yan, R. -H. Ourmazd, A. & Lee, K. F. Scaling the Si MOSFET: From bulk to SOI to bulk. *IEEE Trans. Electron Devices* **39,** 1704–1710 (1992).
3. Santos, E. J. G. & Kaxiras, E. Electric-field dependence of the effective dielectric constant in graphene. *Nano Lett.* **13,** 898–902 (2013).
4. Santos, E. J. G. & Kaxiras, E. Electrically driven tuning of the dielectric constant in MoS$_2$ layers. *ACS nano* **7,** 10741–10746 (2013).
5. Radisavljevic, B. *et al.* Single-layer MoS$_2$ transistors. *Nature Nanotech.* **6,** 147–150 (2011).
6. Li, S.-L. *et al.* Thickness-dependent interfacial coulomb scattering in atomically thin field-effect transistors. *Nano Lett.* **13,** 3546–3552 (2013).
7. Li, L. *et al.* Black phosphorus filed-effect transistors. *Nature Nanotech.* **9,** 372–377 (2014).
8. Liu, H. *et al.* Phosphorene: An unexplored 2D Semiconductor with a high hole mobility. *ACS nano* **8,** 4033–4041 (2014).
9. Feng, W., Zheng, W., Cao, W. & Hu, P. Back gated multilayer InSe transistors with enhanced carrier mobilities via the suppression of carrier scattering from a dielectric interface. *Adv. Mater.* **26,** 6587–6593 (2014).
10. Zhu, W., Perebeinos, V., Freitag, M. & Avouris, P. Carrier scattering, mobilities, and electrostatic potential in monolayer, bilayer, and trilayer graphene. *Phys. Rev. B* **80,** 235402 (2009).
11. Low, T. *et al.* Tunable optical properties of multilayer black phosphorus thin films. *Phys. Rev. B* **90,** 075434 (2014).
12. Peelaers, H. & Van de Walle, C. G. Effects of strain on band structure and effective masses in MoS$_2$. *Phys. Rev. B* **86,** 241401(R) (2012).
13. Oostinga, J. B., Heersche, H. B., Liu, X., Morpurgo, A. F. & Vandersypen, M. K. Gate-induced insulating state in bilayer graphene devices. *Nature Mater.* **7,** 151–157 (2008).
14. Zhang, Y. *et al.* Direct observation of a widely tunable bandgap in bilayer graphene. *Nature* **459,** 820–823 (2009).
15. Miyazaki, H., Tsukagoshi, K., Kanda, A., Otani, M. & Okada, S. Influence of disorder on conductance in bilayer graphene under perpendicular electric field. *Nano Lett.* **10,** 3888–3892 (2010).
16. Xia, F., Farmer, D. B., Lin, Y. -M. & Avouris, P. Graphene field-effect transistors with high on/off current ratio and large transport band gap at room temperature. *Nano Lett.* **10,** 715–718 (2010).

17. Taychatanapat, T. & Jarillo-Herrero, P. Electronic transport in dual-gated bilayer graphene at large displacement fields. *Phys. Rev. Lett.* **105,** 16601 (2010).
18. Zou, K. & Zhu, J. Transport in gapped bilayer graphene: The role of potential fluctuations. *Phys. Rev. B* **82,** 081407(R) (2010).
19. Yan, J. & Fuhrer, M. S. Charge transport in dual gated bilayer graphene with corbino geometry. *Nano Lett.* **10,** 4521–4525 (2010).
20. Szafranek, B. N., Schall, D., Otto, M., Neumaier, D. & Kurz, H. Electrical observation of a tunable band gap in bilayer graphene nanoribbons at room temperature. *Appl. Phys. Lett.* **96,** 112103 (2010).
21. Yu, W. J., Liao, L., Chae, S. H., Lee, Y. H. & Duan, X. Toward tunable band gap and tunable Dirac point in bilayer graphene with molecular doping. *Nano Lett.* **11,** 4759–4763 (2011).
22. Szafranek, B. N., Schall, D., Neumaier, D. & Kurz, H. High on/off ratios in bilayer graphene field effect transistors realized by surface doping. *Nano Lett.* **11,** 2640–2643 (2011).
23. Szafranek, B. N., Fiori, G., Schall, D., Neumaier, D. & Kurz, H. Current saturation and voltage gain in bilayer graphene field effect transistors. *Nano Lett.* **12,** 1324–1328 (2012).
24. Lee, K., Fallahazad, B., Min, H. & Tutuc, E. Transport gap in dual-gated graphene bilayers using oxides as dielectrics. *IEEE Trans. Electron Devices* **60,** 103–108 (2013).
25. Ohta, T., Bostwick, A., Seyller, T., Horn, K. & Rotenberg, E. Controlling the electronic structure of bilayer graphene. *Science* **313,** 951–954 (2006).
26. Mak, K. F., Lui, C. H., Shan, J. & Heinz, T. F. Observation of an electric-field-induced band gap in bilayer graphene by infrared spectroscopy. *Phys. Rev. Lett.* **102,** 256405 (2009).
27. Kuzmenko, A. B. *et al.* Infrared spectroscopy of electronic bands in bilayer graphene. *Phys. Rev. B* **79,** 115441 (2009).
28. Nishi, Y. Study of silicon-silicon dioxide structure by electron spin resonance I. *Jpn. J. Appl. Phys.* **10,** 52–62 (1971).
29. Poindexter, E. H., Caplan, P. J., Deal, B. E. & Razouk, R. R. Interface states and electron spin resonance centers in thermally oxidized (111) and (100) silicon wafers. *J. Appl. Phys.* **52,** 879–884 (1981).
30. Poindexter, E. H. MOS interface states: overview and physicochemical perspective. *Semicond. Sci. Technol.* **4,** 961–969 (1989).
31. Fang, T., Konar, A., Xing, H. & Jena, D. Carrier statistics and quantum capacitance of graphene sheets and ribbon. *Appl. Phys. Lett.* **91,** 092109 (2007).
32. Ye, J. *et al.* Accessing the transport properties of graphene and its multilayers at high carrier density. *Proc. Natl. Acad. Sci. USA* **108,** 13002–13006 (2011).
33. Young, A. F. *et al.* Electronic compressibility of layer-polarized bilayer graphene. *Phys. Rev. B* **85,** 235458 (2012).
34. Henriksen, E. A. & Eisenstein, J. P. Measurement of the electronic compressibility of bilayer graphene. *Phys. Rev. B* **82,** 041412(R) (2010).
35. Kanayama, K., Nagashio, K., Nishimura, T. & Toriumi, A. Large Fermi energy modulation in graphene transistors with high-pressure O_2-annealed Y_2O_3 topgate insulators. *Appl. Phys. Lett.* **104,** 083519 (2014).
36. Nagashio, K., Yamashita, T., Nishimura, T., Kita, K. & Toriumi, A. Electrical transport properties of graphene on SiO_2 with specific surface structures. *J. Appl. Phys.* **110,** 024513 (2011).
37. Koshino, M. Electronic transport in bilayer graphene. *New J. Phys.* **11,** 095010 (2009).
38. Nagashio, K., Nishimura, T. & Toriumi, A. Estimation of residual carrier density near the Dirac point in graphene through quantum capacitance measurement. *Appl. Phys. Lett.* **102,** 173507 (2013).
39. Young, A. F. & Levitov, S. Capacitance of graphene bilayer as a probe of layer-specific properties. *Phys. Rev. B* **84,** 085441 (2011).
40. Farmer, D. B., Lin, Y. -M. & Avouris, P. Graphene field-effect transistors with self-aligned gates. *Appl. Phys. Lett.* **97,** 013103 (2010).
41. Wouters D. J., Colinge J. -P. & Maes, H. E. Subthreshold slope in thin-film SOI MOSFET's. *IEEE Trans. Electron Devices* **37,** 2022–2033 (1990).
42. Nicolian, E. H. & Brews, J. R. *MOS Physics and Technology.* Wiley, New York, 1982.
43. Zhu, W. *et al.* Electronic transport and device prospects of monolayer molybdenum disulphide grown by chemical vapor deposition. *Nature Communications* **5,** 3087 (2014).
44. White, M. H. & Cricchi, J. R. Characterization of Thin-oxide MNOS memory transistors. *IEEE Trans. Electron Devices* **19,** 1280–1288 (1972).
45. Takei, K. *et al.* High quality interfaces of InAs-on-insulator filed-effect transistors with ZrO_2 gate dielectrics. *Appl. Phys. Lett.* **102,** 153513 (2013).
46. Yuan, Y. *et al.* A distributed bulk-oxide trap model for Al_2O_3 InGaAs MOS devices. *IEEE Trans. Electron devices* **59,** 2100–2106 (2012).
47. Kim, K. S. *et al.* Coexisting massive and massless Dirac fermions in symmetry-broken bilayer graphene. *Nature Mater.* **12,** 887–892 (2013).
48. Lin, J. *et al.* AC/AB stacking boundaries in bilayer graphene. *Nano Lett.* **13,** 3262–3268 (2013).
49. Koshino, M. Electronic transmission through AB-BA domain boundary in bilayer graphene. *Phys. Rev. B* **88,** 115409 (2013).
50. Heiman, F. P. & Warfield, G. The effect of oxide traps on the MOS capacitance. *IEEE Trans. Electron Devices* **12,** 167–178 (1965).
51. Mott, N. F. & Davis, E. A. *Electronic processes in non-crystalline materials.* Clarendon press, Oxford, 1971.
52. Li, W. *et al.* Ultraviolet/ozone treatment to reduce metal-graphene contact resistance. *Appl. Phys. Lett.* **102,** 183110 (2013).

Author Contributions

K.N. conceived the experiment. K.K. and K.N. fabricated the devices, carried out the measurements and performed data analysis. K.N. wrote the manuscript.

Additional Information

Supplementary information accompanies this paper at http://www.nature.com/srep

Competing financial interests: The authors declare no competing financial interests.